Supporting Information

Exploration of Near-Infrared-Emissive Colloidal Multinary Lead Halide Perovskite Nanocrystals using an Automated Microfluidic Platform

Ioannis Lignos,[1] Viktoriia Morad,[1,2,3] Yevhen Shynkarenko,[2,3] Caterina Bernasconi,[2,3] Richard M. Maceiczyk,[1] Loredana Protesescu,[2,3] Federica Bertolotti,[4,5] Sudhir Kumar,[1] Stefan T. Ochsenbein,[2,3] Norberto Masciocchi,[4] Antonietta Guagliardi,[6] Chih-Jen Shih,[1] Maryna I. Bodnarchuk,[3*] Andrew J. deMello[1*] and Maksym V. Kovalenko[2,3*]

1Institute for Chemical and Bioengineering, Department of Chemistry and Applied Biosciences, ETH Zürich, Vladimir-Prelog-Weg 1, 8093, Switzerland

[2]Institute of Inorganic Chemistry, Department of Chemistry and Applied Biosciences, Vladimir-Prelog-Weg 1, 8093, Switzerland

[3]Empa-Swiss Federal Laboratories for Materials Science and Technology, Überlandstrasse 129, 8600, Switzerland

[4]Dipartimento di Scienza e Alta Tecnologia and To.Sca.Lab, Università dell'Insubria, via Valleggio 11, I-22100 Como, Italy

[5]Aarhus Institute of Advanced Studies (AIAS), Aarhus University, Høegh-Guldbergs Gade 6B, 8000 Aarhus C, Denmark.

[6]Istituto di Crystallografia and To.Sca.Lab, Consiglio Nazionale delle Ricerche, via Valleggio 11, I-22100 Como, Italy

*andrew.demello@ethz.ch, *mvkovalenko@ethz.ch, *maryna.bodnarchuk@empa.ch

Preparation of precursors for the synthesis of $Cs_xFA_{(1-x)}PbI_3$ and $Cs_xFA_{1-x}Pb(Br_{1-y}I_y)_3$ nanocrystals.

"Standard Precursors"

Preparation of Cs-oleate: Cesium carbonate (0.6 mmol, Sigma-Aldrich, 99.9%) was loaded into a 100 mL Schlenk flask along with OA (2.5 mL, Sigma-Aldrich, 90%) and degassed ODE (40 mL, Sigma-Aldrich, 90%). The mixture was degassed for 30 min at room temperature and then heated under N_2 to 130 °C until the reaction completed. The solution was cooled and stored under argon for several days without precipitation at room temperature.

Preparation of FA-oleate: Formamidinium acetate (1.24 mmol, Sigma-Aldrich, 99.9%) was loaded into a 100 mL Schlenk flask along with OA (4 mL, Sigma-Aldrich, 90%) and degassed ODE (16 mL, Sigma-Aldrich, 90%). The mixture was degassed for 30 min at room temperature and then heated under N_2 to 130 °C until the reaction completed. The solution was cooled and stored under argon for several days without precipitation at room temperature.

Preparation of lead halide solution: PbX_2 salts such as $PbBr_2$ (0.048 mmol, ABCR, 98%) and PbI_2 (0.193 mmol, ABCR, 99.999%) were added in a 20 mL Schlenk flask together with dried ODE (5 mL). The mixture was then dried under vacuum for 30 min at 60 °C. After 2 h, 1 mL of dried OA and 0.5 mL dried OLA were added under argon until all PbX_2 dissolved completely.

"OA-rich precursors"

The methodology for the preparation of precursor solutions was the same. Variations of precursor quantities are the following:

- Cs-oleate precursor solution contained 2.5 mmol of Cs_2CO_3 in 40 ml of ODE and 8 ml of OA;
- FA-oleate precursor was prepared as 5 mmol of FA-acetate in 16 ml of ODE and 8 ml of OA;
- PbI_2 precursor was prepared as 0.193 mmol of PbI_2 in 5 ml ODE with 1 ml of OA and 0.5 ml of OLA.

"Low-concentration precursors"

Other variations of FA-oleate and Cs-oleate were used to improve precursors' stability and aimed to reach low contents of Cs incorporation:

- FA-oleate precursor was prepared as 0.63 mmol of FAAc in 6 ml of ODE and 4 ml of OA;
- Cs-oleate precursor was prepared as $0.6/n$ mmol of Cs_2CO_3 in 10 ml of ODE and 0.625 ml of OA, where n was 4, 10, 20, 40 depending on the aim of the experiment.

Purification after microfluidic synthesis for offline measurements (XRD, TEM): 1-3 ml of crude solution was centrifuged for 3 min at 12 krpm, the supernatant was discarded and the precipitate was dissolved in toluene. After addition of antisolvent (CH_3CN, 1:10 v/v), the solution was centrifuged for 90 seconds at 12 krpm. Supernatant was discarded and precipitate redispersed in 3 ml of toluene. The cycle was repeated several times if needed.

Data processing and analysis: The systematic mapping of reaction parameters was performed using our automated droplet-based microfluidic platform. Initially a file with all the different precursor combinations, temperatures and reaction times is loaded into an in-house Labview automated program. The microfluidic platform performs all expected reactions in an autonomous way and PL spectra are recorded in an output file. Each spectrum was generated from a weighted average of 100-300 scans with an integration time of 50 ms. To precisely define the absorption peak, the second derivative of the absorption spectrum was calculated.

Modelling of the total scattering data through the Debye Scattering Equation (DSE) approach

In order to perform the structural and microstructural characterization of $Cs_xFA_{1-x}(Br_{1-y}I_y)_3$ we used a total scattering approach based on a fast implementation of the DSE, in which, with appropriate adjustments,[1] the use of this (in principle) highly time-consuming approach, is made feasible. The DSE[2] describes the differential cross section of a randomly oriented powder and allows the simultaneous modelling of the Bragg and diffuse scattering as a function of the interatomic distances within the nanoparticle:

$$I(Q) = \sum_{j=1}^{N} f_j(Q)^2 o_j^2 + 2\sum_{j>i}^{N} f_j(Q) f_i(Q) T_j(Q) T_i(Q) o_j o_i \frac{\sin(Q d_{ij})}{(Q d_{ij})}$$

where $Q = \frac{4\pi sin\theta}{\lambda}$ is the magnitude of the scattering vector, λ is the radiation wavelength, f_{ij} is the X-ray atomic form factor, d_{ij} is the interatomic distance between atoms i and j, N is the total number of atom and T and o are the thermal atomic displacement parameter and site occupancy factor associated to each atomic species, respectively.

The approach used in this work is the one implemented in the *DebUsSy* Suite of programs,[3] which use the sampled interatomic distances instead of the original ones in order to speed up calculations.

The modelling strategy used in this work can be summarized, as follows:

i) a bottom up approach was used to generate the bivariate population of atomistic models of nanocrystals according to two independent growing directions, one along the *c*-axis and the other one parallel to the *ab*-plane. A primitive cubic unit cell (SG. *Pm-3m*) was used as the building block for generating atomistic models of $Cs_xFA_{1-x}(Br_{1-y}I_y)_3$ NCs, in which the perovskite framework is made by PbX_6 units, sharing the octahedra corners and the X anions are disordered in four equivalent positions (Pb-X-Pb bond angles deviates from their ideal 180° of ca. 15°). Resorting to this cubic structure with 24 disordered X anions surrounding each Pb (*cubic-splitted* model, reported in the inset of Figure 5d of the main text), is justified but the abnormally high atomic displacement parameters found for X that suggests the occurrence of a local displacement of these ions with respect to the ideal cubic position (B(X) = 4.80 $Å^2$ in the refined cubic model *vs.* 0.44 $Å^2$ of the "*splitted*" one). The same structure was already used for modelling the synchrotron experimental data of $FAPbBr_3$[4] and $FAPbI_3$[5] colloidal NCs.

The FA^+ cation is disordered inside the cuboctahedral cavities and a single pseudo –atom with atomic scattering factor equal to the one of the whole molecule was used in the modeling, due to the difficulties in determining the coordinates of the disordered C/H atoms of FA using X-ray powder diffraction. The outer organic oleate shell, nearly invisible at X-rays, was neglected in our atomistic models.

ii) The sampled interatomic distances of the NCs were computed and stored in suitable databases, in order to calculate the DSE model, used in the next step.

iii) The refinement of the model pattern against the experimental data, involving a number of adjustable parameters, was performed. To account for size and shape distribution of the bivariate populations of $Cs_xFA_{1-x}(Br_{1-y}I_y)_3$ NCs, a bivariate log-normal function with five adjustable parameters (the average and standard deviation parameters for the distributions along the two growing directions and the correlation angle between them) was used.

The graphical outcomes of the DSE-based analysis on $Cs_xFA_{1-x}(Br_{1-y}I_y)_3$ are summarized in Figure S13. The quality of the best fit of the solvent-subtracted data reported in Figure S13a suggests the presence of some residual structural distortion, as much as recently reported for all-inorganic lead halide perovskite NCs.[6] Analogously to the case of $CsPbX_3$ NCs, peak positions slightly deviate from the cubic metric; nevertheless the hybrid NCs here investigated exhibit a different kind of structural defectiveness, which needs further investigations.

Isotropic atomic displacements parameters were refined for all the atoms. In order to investigate the substitutional disorder between the $FA_{(1-x)}/Cs_x$ and $Br_{(1-y)}/I_y$ couples the corresponding site occupancies factors (s.o.f.) were refined through a conventional Rietveld method using the TOPAS-R program,[7] and the resulting values (x=0; y=0.87) were kept fix during the DSE-based modeling.

Although the Cs quantity resulted too low to be detected through this technique, we cannot exclude that very few amount of this cation (< 5 %) might be present in the crystal structure.

Moreover, the refined s.o.f. value of Br is well in agreement with that derived upon adoption of Vegard's Law, linearly correlating the refined lattice parameter and the anionic composition of $Cs_xFA_{1-x}(Br_{1-y}I_y)_3$ (a = 6.3296 Å) with the two (Cs-free) end members of the same series ($FAPbI_3$ and $FAPbBr_3$, Figure S14); this estimate has also been confirmed by independent X-ray fluorescence measurements, giving a s.o.f.(Br) = 0.16(3).

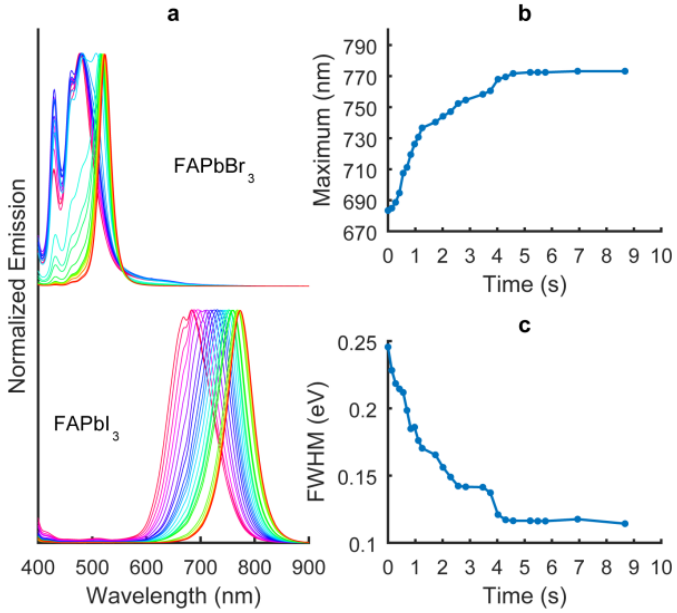

Figure S1: (a) Evolution of PL spectra during the synthesis of $FAPbBr_3$ and $FAPbI_3$ at 80°C. Time dependence of emission maximum (b) and FWHM (c) for $FAPbI_3$ synthesis.[8]

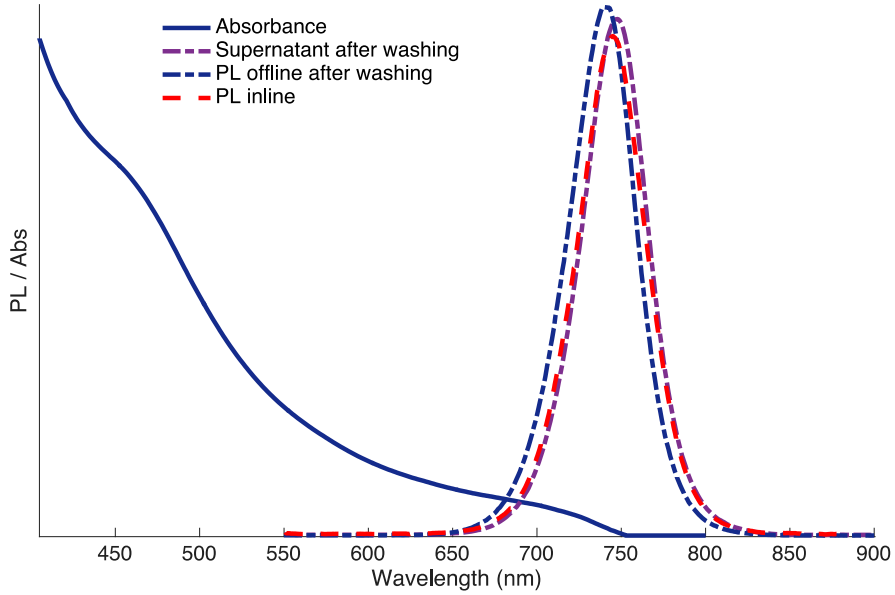

Figure S2: PL and absorbance spectra of $Cs_xFA_{1-x}PbI_3$ NCs, which were recorded in-line and offline (before and after particle purification) confirming that there is no subsequent growth after 7s of reaction at 80 °C. FA/Pb ratio is 14:1, Cs/Pb ratio is 0.5:1 and Cs% is 3.6.

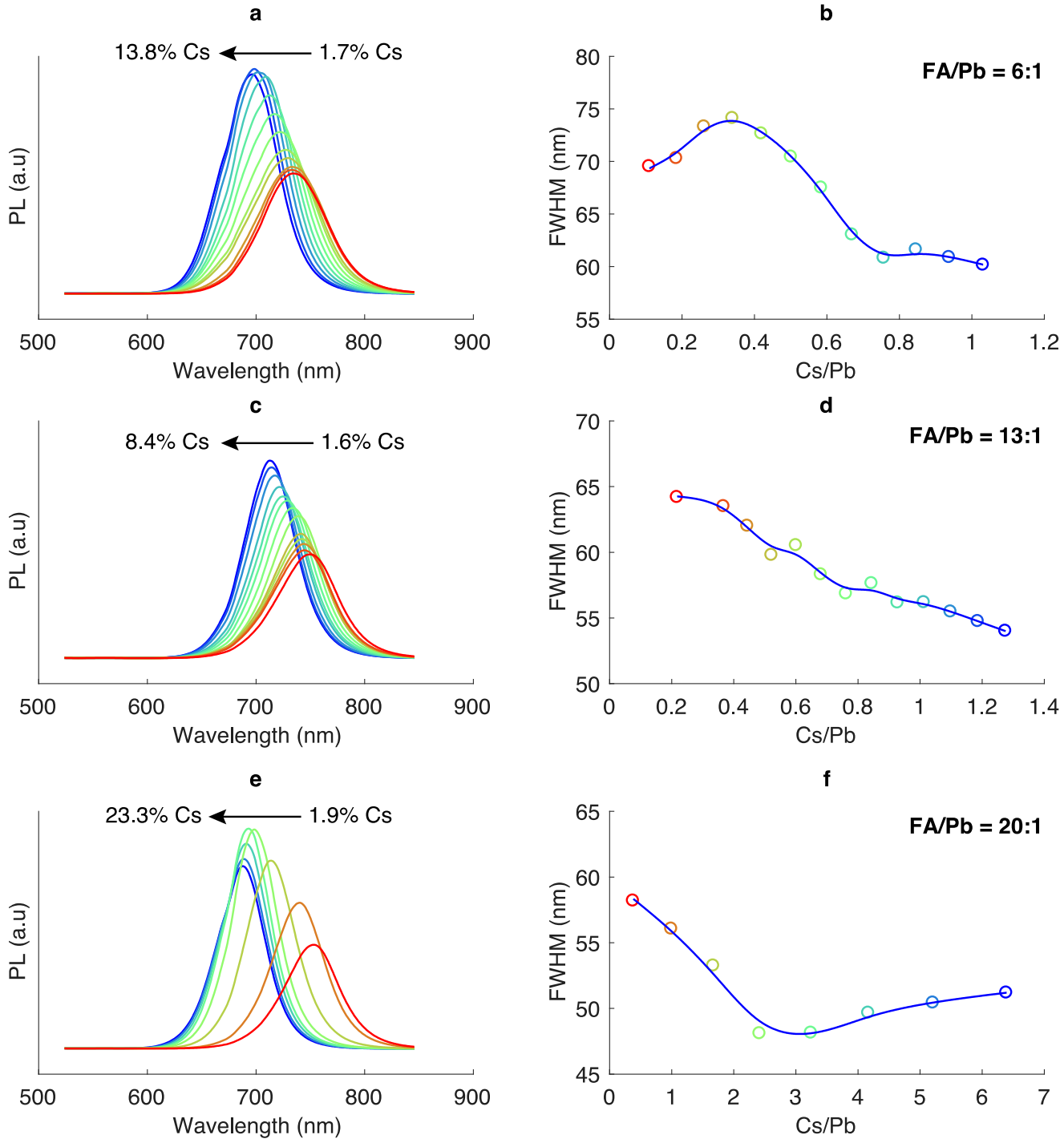

Figure S3: Effect of the Cs-to-Pb molar ratio on PL spectra and FWHM of $Cs_xFA_{1-x}PbI_3$ NCs for various FA to Pb molar ratios. Colors in the PL spectra and data markers displayed in Figures S3b,d,f correspond to various Cs loadings indicated in the corresponding legends. The temperature (80 °C) and reaction time (7 s) were maintained constant.

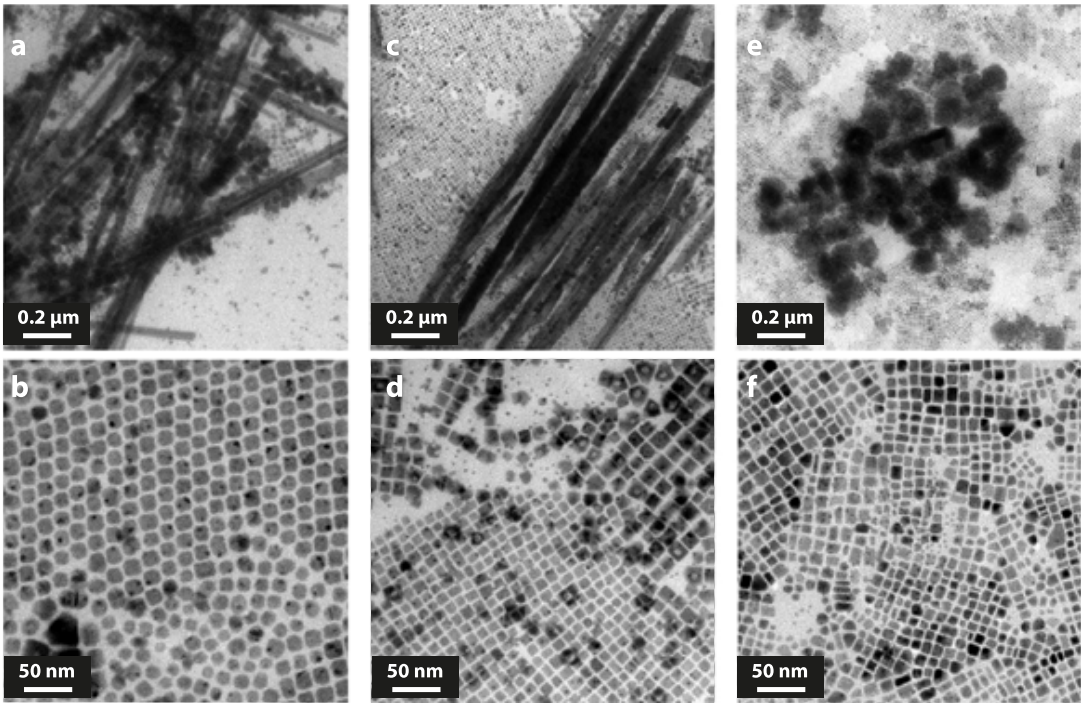

Figure S4: TEM images of $Cs_xFA_{1-x}PbI_3$ NCs while altering the FA to Pb molar ratio. (a-b) FA/Pb = 20, (c-d) FA/Pb = 13, (e-f) FA/Pb = 6.

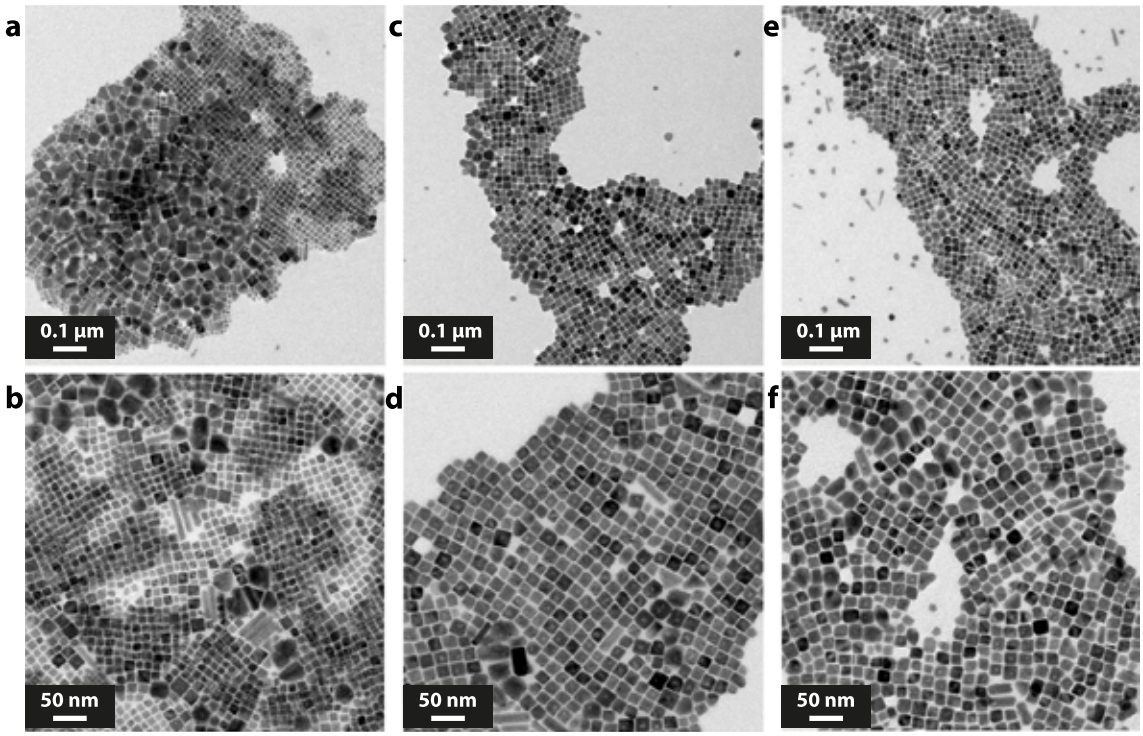

Figure S5: TEM images of $Cs_xFA_{1-x}PbI_3$ NCs while altering the Cs to Pb molar ratio. (a-b) Cs/Pb = 0.4, (c-d) Cs/Pb = 0.55, (e-f) Cs/Pb = 0.7.

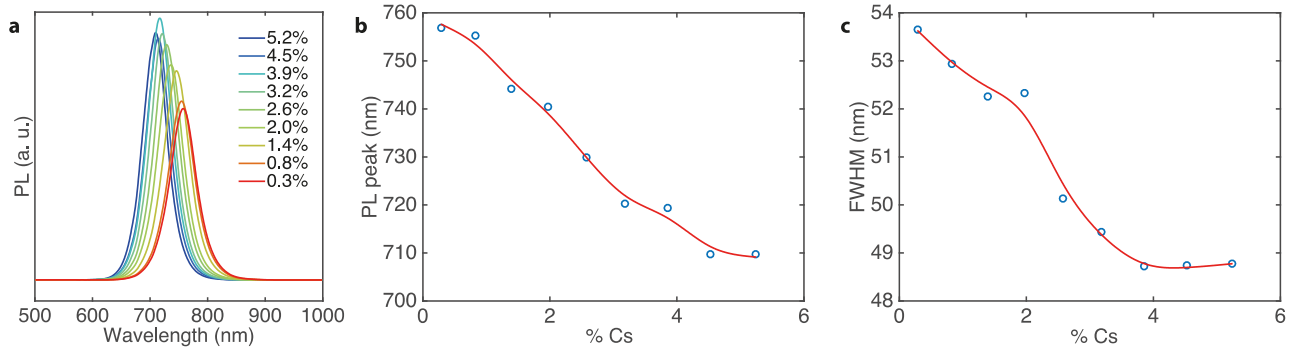

Figure S6: Tuning of the (a) emission spectra, (b) PL peak wavelength, (c) FWHM of $Cs_xFA_{1-x}PbI_3$ NCs by varying the Cs content (0.3-5.2%). Other parameters were: T = 80 ºC, time = 7 s, FA/Pb = 14, Cs/Pb = 0.05-0.81.

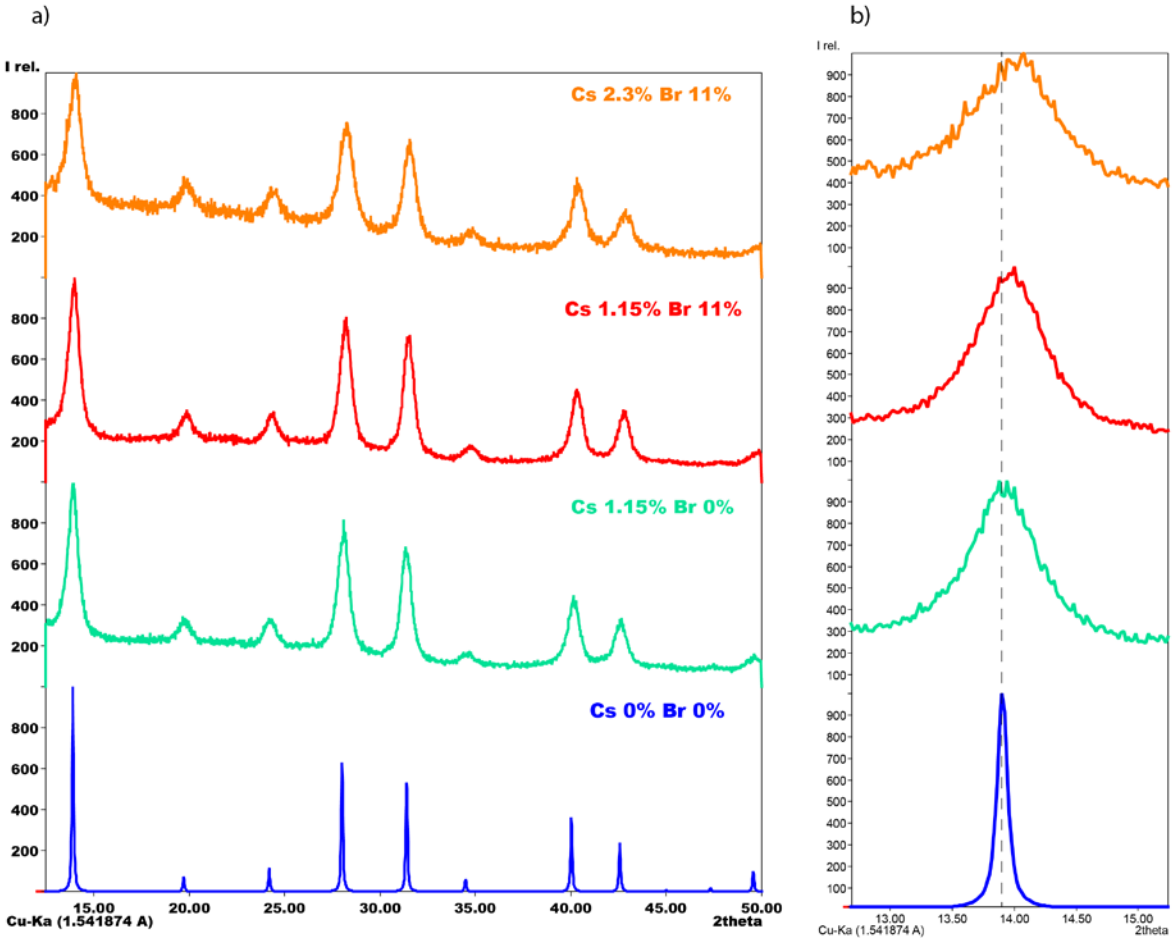

Figure S7: XRD patterns of $Cs_xFA_{1-x}Pb(Br_{1-y}I_y)_3$ NCs synthesized in the microfluidic platform which were collected from toluene solutions.

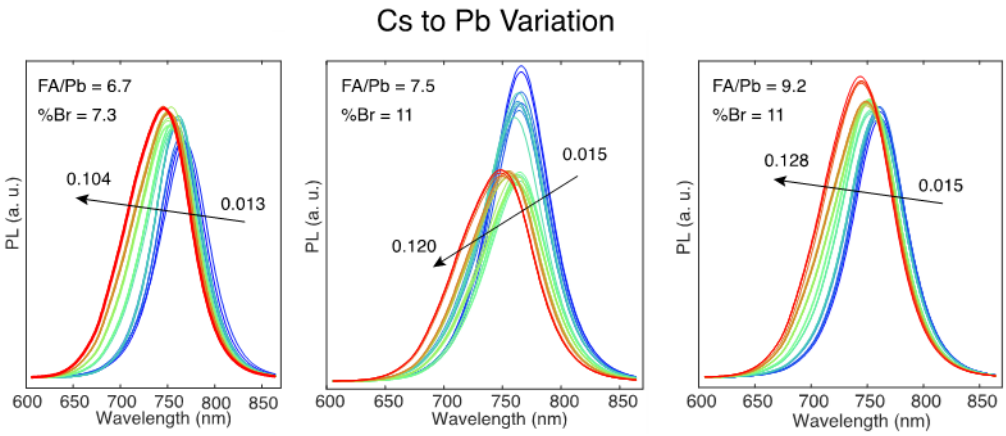

Figure S8: Effect of the Cs to Pb molar ratio on PL spectra of $Cs_xFA_{1-x}Pb(Br_{1-y}I_y)_3$ NCs for various FA-to-Pb molar ratios and Br loadings. Colors in the PL spectra correspond to various Cs to Pb ratios indicated in the arrow limits.

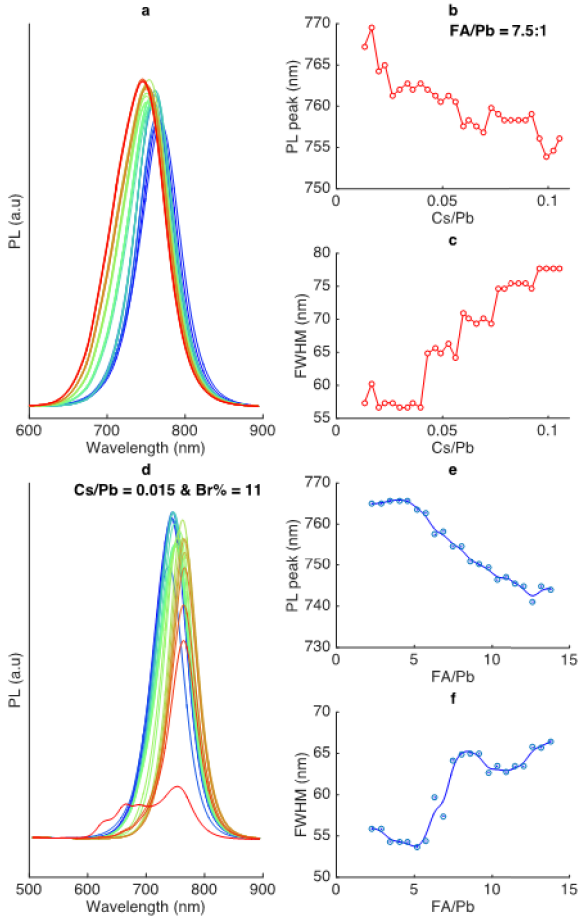

Figure S9: (a-c) Effect of the Cs to Pb molar ratio on the PL characteristics of $Cs_xFA_{1-x}Pb(Br_{0.12}I_{0.88})_3$ NCs. Other parameters were FA/Pb = 7.5 and Cs loading from 0.2 – 1.4%. (d-f) Evolution of PL features of $Cs_xFA_{1-x}Pb(Br_{0.11}I_{0.89})_3$ NCs by a systematic variation of FA/Pb. Other parameters were Cs/Pb = 0.015 and Cs loading from 0.1 – 1.1%.

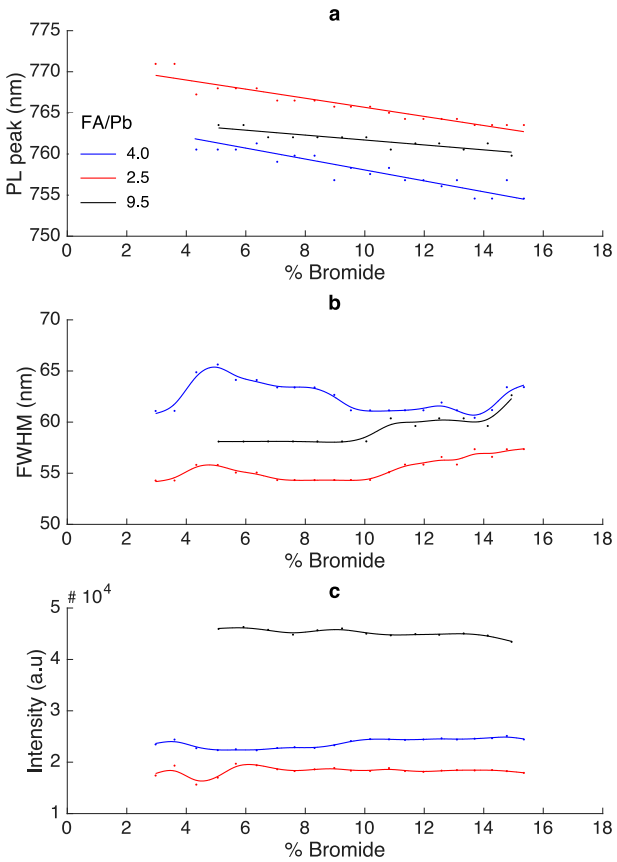

Figure S10: Evolution of (a) PL peak, (b) FWHM, and (c) maximum PL intensity of $Cs_xFA_{1-x}Pb(Br_{1-y}I_y)_3$ NCs by increasing the Br loading from 3-15%. For all experimental sets Cs to Pb molar ratio was equal to 0.015.

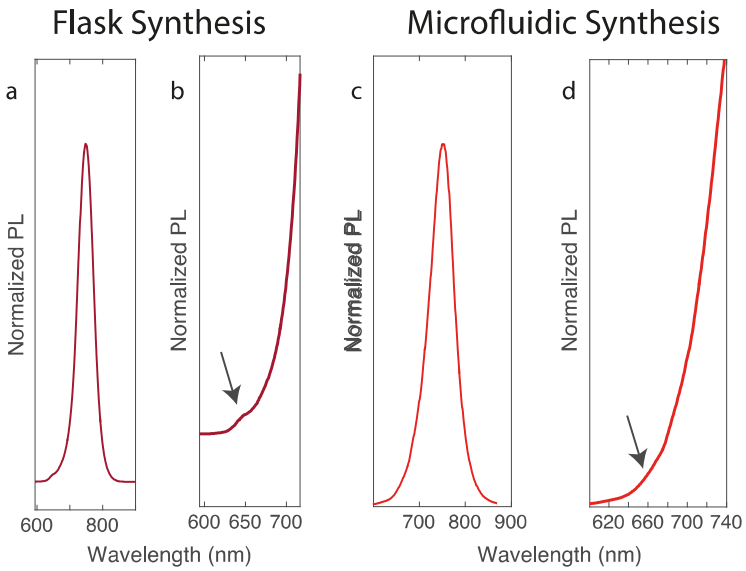

Figure S11: Synthesis of $Cs_{0.01}FA_{0.99}Pb(Br_{0.15}I_{0.85})_3$ NCs in a flask and a microfluidic reactor. (a) PL spectrum of the NCs emitting at 750 nm synthesized in a flask reactor, (b) the arrow indicates the second PL peak at 640 nm which could correspond to the formation of $FAPb(Br_{1-y}I_y)_3$ NCs, (c) PL spectrum of the NCs emitting at 750 nm synthesized in a microfluidic reactor, (b) the arrow indicates the second PL peak at 650-660 nm which again corresponds to the concurrent formation of $FAPb(Br_{1-y}I_y)_3$ NCs. Other experimental parameters were: FA/Pb = 4.9, Cs/Pb = 0.068, %Cs = 1.15%, %Br = 15%.

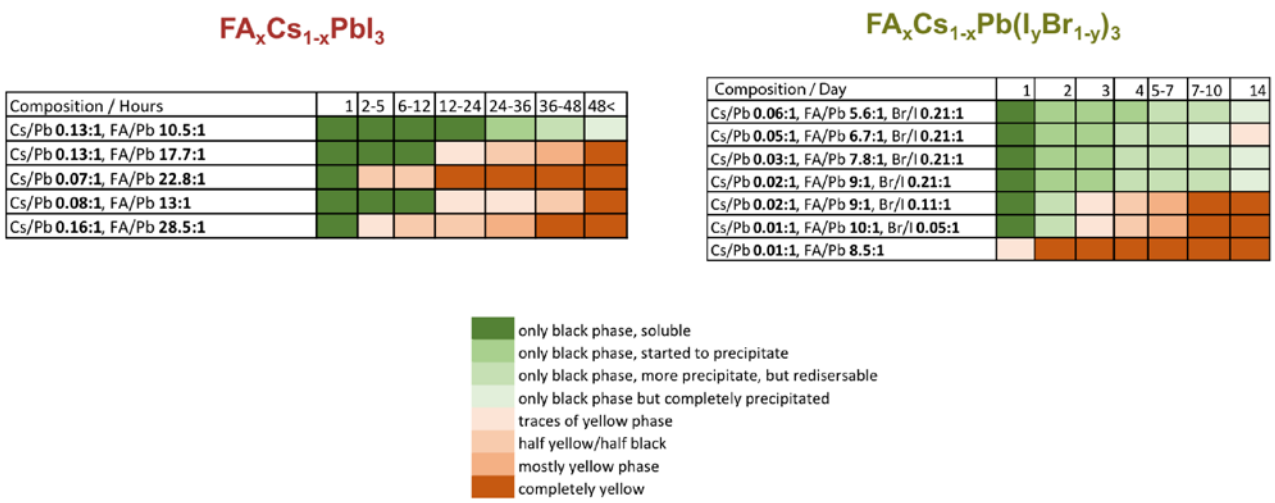

Figure S12: Overview of the stability measurements for $Cs_xFA_{1-x}PbI_3$ and $Cs_xFA_{(1-x)}Pb(Br_{y-1}I_y)_3$ NCs synthesized in the microfluidic platform over several weeks. The tables indicate the colloidal stability and phase stability of the samples.

a)

b)

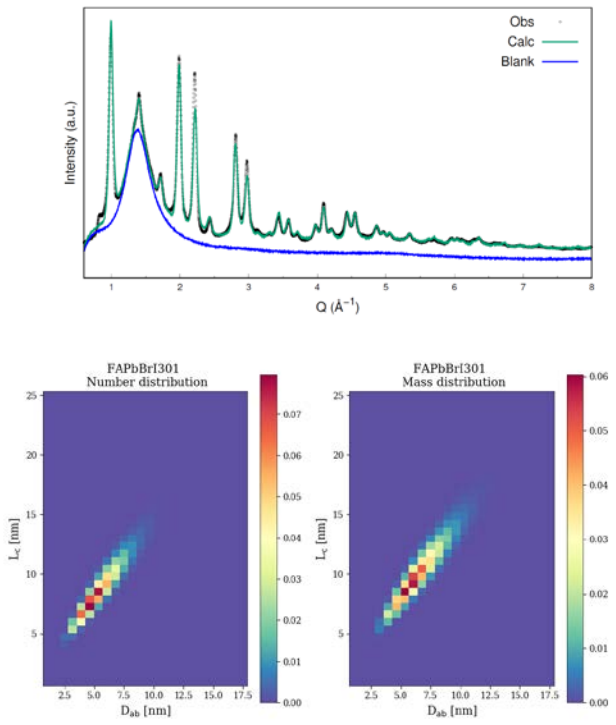

Figure S13: *(*a) Best fit of the synchrotron X-ray total scattering data of $Cs_xFA_{1-x}Pb(Br_{y-1}I_y)_3$ using the *cubic-splitted* model. The blue trace is the octane solvent. (b) 2D maps in the L_c and D_{ab} coordinates (L_c is the length along the c-axis, D_{ab} is the diameter of the circle of equivalent area in the ab-plane) of the bivariate (number-based) Log-normal size distributions. Average number-based diameter of the sphere of equivalent volume: $\langle D_{eq} \rangle$ = 7.80 nm; $\sigma/\langle D_{eq} \rangle$ = 0.24 nm. Average number -based sizes along the two growing directions: $\langle D_{ab} \rangle$ = 5.91 nm ; $\sigma/\langle D_{ab} \rangle$ = 0.25 ; $\langle L_c \rangle$ = 9.05 nm; $\sigma/\langle L_c \rangle$ = 0.22. Aspect ratio ($\langle L_c \rangle/\langle D_{ab} \rangle$) = 1.53.

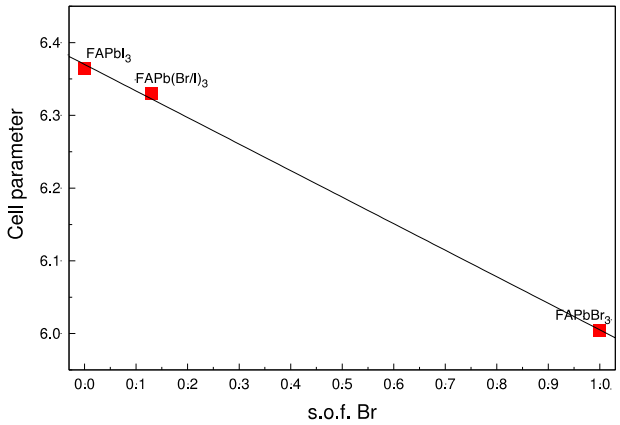

Figure S14: Site occupancy factor (s.o.f.) of Br determined using X-ray total scattering data for three FAPbX3 samples (with X=I, Br/I, Br) as red squares and the related fit (solid line) obtained through the Vegard Law for solid solutions and alloys: $a_{Br} = x a_{FAPbBr_3} + (1-x) a_{FAPbI_3}$ (where a is the lattice parameter, determined for each sample). As shown here the intermediate point (FAPb(Br/I)3, a = 6.3296 Å) between the two reference values (FAPbI3 a = 6.3639 Å and FAPbBr3 a = 6.0042 Å)[4-5] well matches the linear relationship.

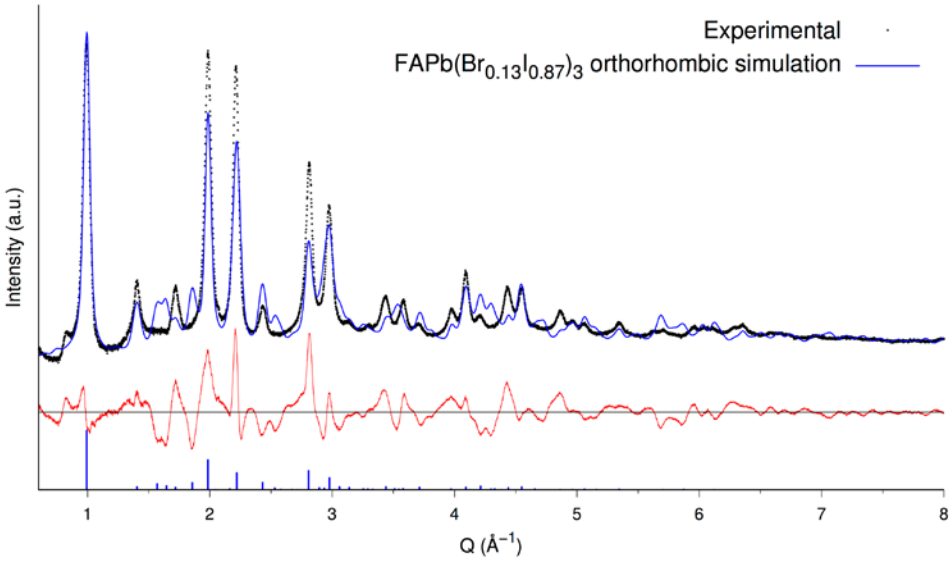

Figure S12: Synchrotron XRD pattern for quinary NCs (black dots) and simulation (blue trace) of $FAPb(Br_{0.13}I_{0.87})_3$ with the orthorhombic (*Pnma*) crystal structure reported by Schueller et al. (stable below 100K). The *Pnma* structure does not reproduce the experimental peak intensities. The new peaks do not have counterpart in the experimental data, thus indicating that the cubic model described above is of much better correspondence to the experiment.

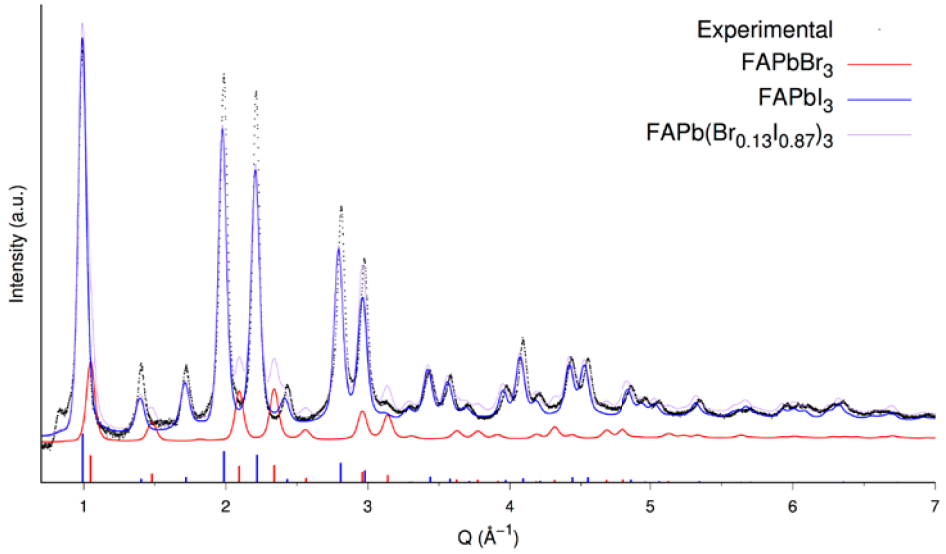

Figure S16: Synchrotron XRD pattern (black dots) $Cs_xFA_{1-x}Pb(Br_{1-y}I_y)_3$ and simulations of $FAPbBr_3$ (red trace), $FAPbI_3$ (blue trace) and their mixture reflecting the Br/I compositions (magenta trace), all in cubic phase. The splitting of the peaks at low angle and the shift at high angle are not in agreement with the experimental data, confirming the formation of a solid solution in multinary NCs studied in this work.

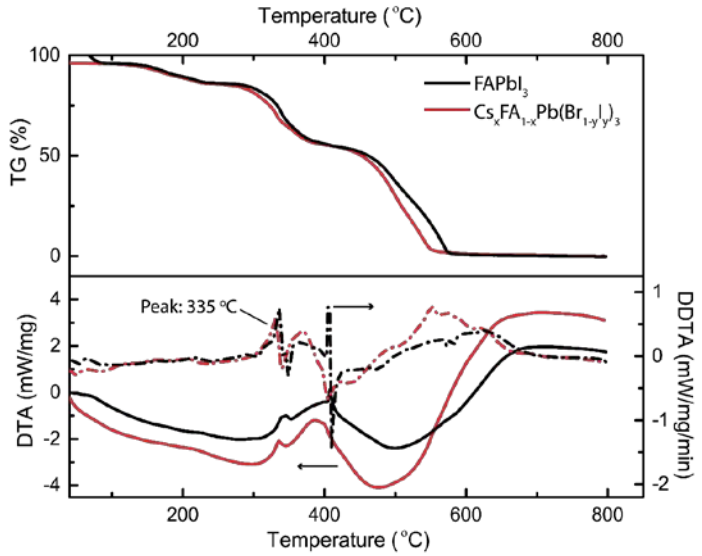

Figure S13: Thermal analysis of $Cs_xFA_{1-x}Pb(Br_{1-y}I_y)_3$ and $FAPbI_3$ NCs: thermogravimetric analysis (TG), differential scanning calorimetry (DSC) and derivative DSC. These results indicate that both materials have very similar thermal stabilities, determined by the inherent chemical stability of the FA cation.

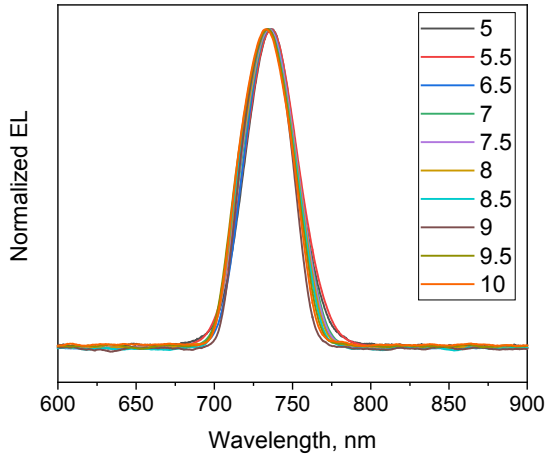

Figure S14: Normalized EL spectra of the champion **device 1** run at various voltages (indicated in Volts on the Figure legend). Peak position varies by no more than 3 nm indicating high stability of the emitting material. FWHM varies from 37 nm to 42 nm.

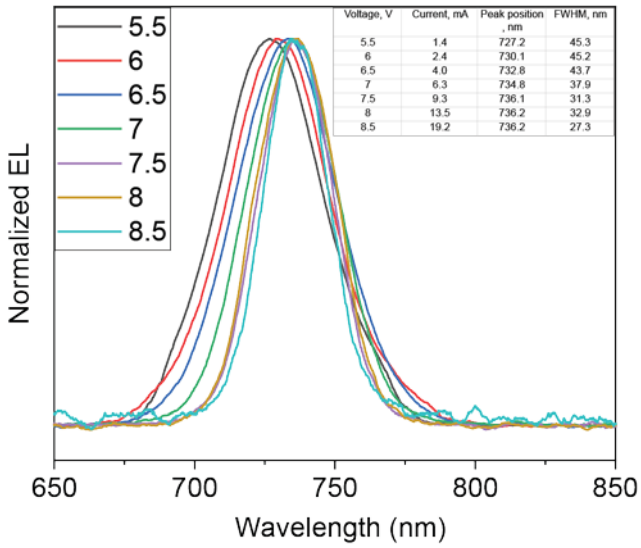

Figure S19: Normalized EL spectra of the **device 2**, where active layer contained small addition of the TOPAS polymer (0.5 mg/ml). El spectra are recorded at various voltages (indicated in Volts on the Figure legend). Narrowing of the EL emission with increasing the voltage and red shift of the emission peak are observed. The inset table shows Gaussian peak fitting parameters for the spectra. Narrowest emission corresponds to 27.3 nm (63 meV) at 736 nm. The EQE of the device was 4.2%. Such shift could be a sign of the ionic migration at various applied voltages with or without a concomitant energy transfer between NCs (from wider bandgap to lower bandgap NCs).

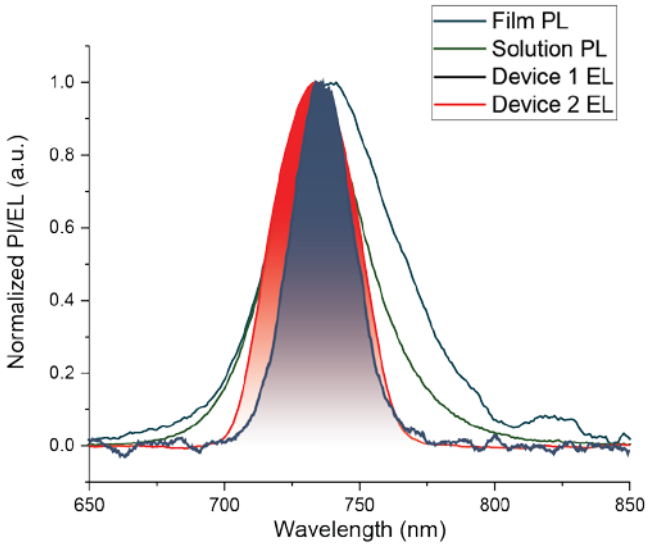

Figure S20. Comparison of the PL of the $Cs_xFA_{1-x}Pb(Br_{1-y}I_y)_3$ NCs in solution (FWHM=40 nm), film (FWHM=52nm) and EL of the device 1 and device 2 (FWHM was 37 and 27 nm, respectively). Both devices showed narrower EL spectra than the corresponding PL spectra of the films and solutions.

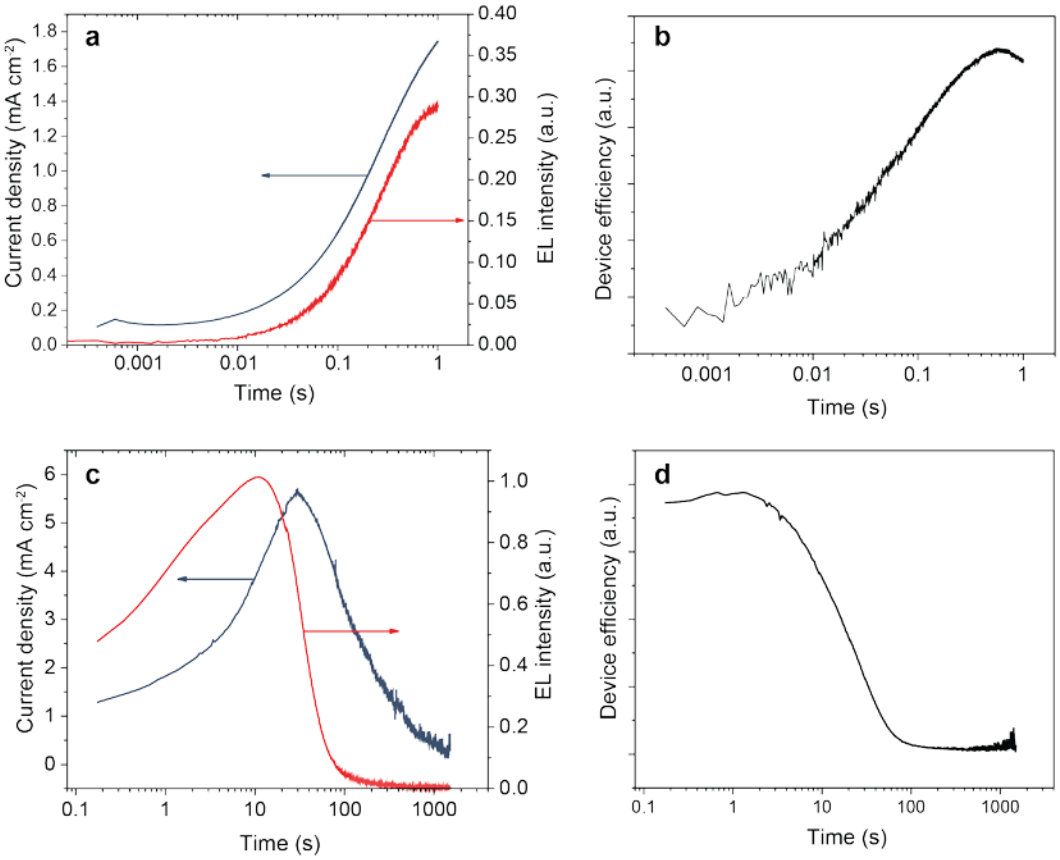

Figure S21. (a) Transient LED response for 1 s voltage pulse of 4.5 V recorded with temporal resolution of 20 us. Continuous growth of current density and EL intensity is observed. However, within the first second, the device efficiency grows as well (b). (c) Operational stability test at a constant voltage of 4.5V and (d) corresponding evolution of the device efficiency. Continuous growth of the device current density and efficiency indicates ionic rearrangement similar to the light emitting electrochemical cells.[9]

References:

1. Cervellino, A.; Giannini, C.; Guagliardi, A., On the Efficient Evaluation of Fourier Patterns for Nanoparticles and Clusters. *J. Comput. Chem.* **2006,** *27*, 995-1008.
2. Debye, P., Zerstreuung von Röntgenstrahlen. *Annalen der Physik* **1915,** *351*, 809-823.
3. Cervellino, A.; Frison, R.; Bertolotti, F.; Guagliardi, A., DEBUSSY 2.0: the New Release of a Debye User System for Nanocrystalline and/or Disordered Materials. *J. Appl. Crystallogr.* **2015,** *48*, 2026-2032.
4. Protesescu, L.; Yakunin, S.; Bodnarchuk, M. I.; Bertolotti, F.; Masciocchi, N.; Guagliardi, A.; Kovalenko, M. V., Monodisperse Formamidinium Lead Bromide Nanocrystals with Bright and Stable Green Photoluminescence. *J. Am. Chem. Soc.* **2016,** *138*, 14202-14205.
5. Protesescu, L.; Yakunin, S.; Kumar, S.; Bar, J.; Bertolotti, F.; Masciocchi, N.; Guagliardi, A.; Grotevent, M.; Shorubalko, I.; Bodnarchuk, M. I.; Shih, C. J.; Kovalenko, M. V., Dismantling the "Red Wall" of Colloidal Perovskites: Highly Luminescent Formamidinium and Formamidinium-Cesium Lead Iodide Nanocrystals. *ACS Nano* **2017,** *11*, 3119-3134.
6. Bertolotti, F.; Protesescu, L.; Kovalenko, M. V.; Yakunin, S.; Cervellino, A.; Billinge, S. J. L.; Terban, M. W.; Pedersen, J. S.; Masciocchi, N.; Guagliardi, A., Coherent Nanotwins and Dynamic Disorder in Cesium Lead Halide Perovskite Nanocrystals. *ACS Nano* **2017,** *11*, 3819-3831.
7. TOPAS-R, V. *TOPAS-R, V.4.0*, Bruker AXS: Karlsruhe, Germany, 2006.
8. Maceiczyk, R. M.; Dümbgen, K.; Lignos, I.; Protesescu, L.; Kovalenko, M. V.; deMello, A. J., Microfluidic Reactors Provide Preparative and Mechanistic Insights into the Synthesis of Formamidinium Lead Halide Perovskite Nanocrystals. *Chem.Mater.* **2017,** *29*, 8433-8439.
9. Meier, S. B.; Tordera, D.; Pertegás, A.; Roldán-Carmona, C.; Ortí, E.; Bolink, H. J., Light-Emitting Electrochemical Cells: Recent Progress and Future Prospects. *Mater. Today* **2014,** *17*, 217-223.